Environmental Functional Materials 4 (2025) 21–32

Contents lists available at ScienceDirect

Environmental Functional Materials

journal homepage: www.keaipublishing.com/en/journals/environmental-functional-materials

Development of ag/Ag_2O/$BiPO_4$/Bi_2WO_6/g-C_3N_4 Z-scheme photocatalyst for high-efficiency tetracycline removal: Characterization, degradation pathway and toxicity assessments

Hongjian Zhang [a], Qiansu Ma [a,b], Guangqi An [a], Yunxin Zhu [a,c], Xiang Sun [a], Naoki Kawazoe [d], Guoping Chen [d], Yingnan Yang [a,*]

[a] Graduate School of Life and Environmental Science, University of Tsukuba, 1-1-1 Tennodai, Tsukuba, Ibaraki, 305-8572, Japan
[b] College of Chemistry and Biological Engineering, University of Science and Technology Beijing, No. 30 Xueyuan Road, Beijing, 100083, PR China
[c] Faculty of Bioenvironmental Sciences, Kyoto University of Advanced Science, 1-1 Sogabecho Nanjo Otani, Kameoka, Kyoto, 621-8555, Japan
[d] Research Center of Macromolecules and Biomaterials, National Institute for Materials Science, 1-1 Namiki, Tsukuba, Ibaraki, 305-0044, Japan

HIGHLIGHTS

- A novel Ag/Ag_2O/$BiPO_4$/Bi_2WO_6/g-C_3N_4 (ABC) photocatalyst was successfully developed.
- Optimized ABC ratio achieved high crystallinity and enhanced photocatalytic activity.
- •O_2^-, h^+, •OH were detected to imply the formation of Z-scheme heterojunction in ABC.
- TC degradation pathway was proposed based on intermediates and DFT calculations.
- ABC showed promise for antibiotic treatment under real environmental conditions.

GRAPHICAL ABSTRACT

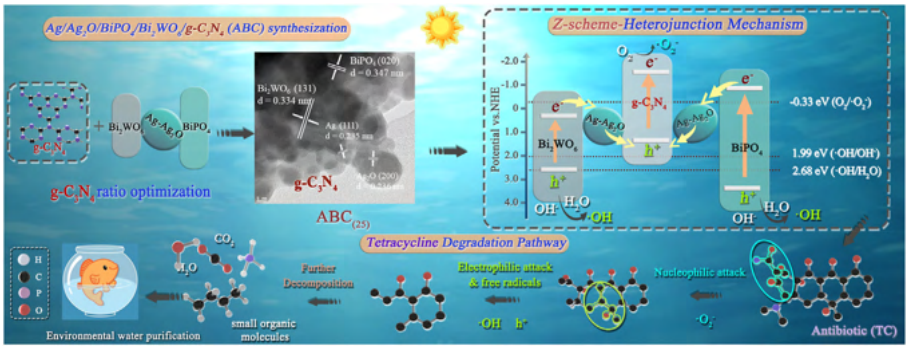

ARTICLE INFO

Keywords:
Photocatalysis
g-C_3N_4 doping
Z-scheme heterojunction
Tetracycline degradation
Intermediates identification

ABSTRACT

Nowadays, tetracycline (TC) contamination of surface water has become a comprehensive environmental problem that threatens the health and survival of animals and humans. It is essential to develop an efficient, and sustainable wastewater treatment strategy. This study introduces a novel Ag/Ag_2O/$BiPO_4$/Bi_2WO_6/g-C_3N_4 (ABC) Z-scheme photocatalyst for high-efficiency TC removal under visible light. Optimized g-C_3N_4 doping facilitated the electron transfer and provided more reaction sites for TC removal. It showed high efficiency, stable TC degradation activity and environmental adaptability. Moreover, the active reaction site on TC was predicted via DFT calculation. In addition, through the analysis of the intermediates identified by LC-MS, the photo-decomposition pathways of TC were proposed. Based on the results of free radical trapping experiments and ESR spectroscopy, the mechanism of TC degradation was suggested. Finally, a toxicity assessment based on the molecular fractals data was carried out. The developed ABC showed higher visible light absorbance, better e^--h^+ separation, and higher phase purity and crystallinity. Overall, this study provides valuable insights into the development of Z-scheme heterojunctions composite for efficient organic pollution degradation.

* Corresponding author.
E-mail address: yo.innan.fu@u.tsukuba.ac.jp (Y. Yang).
Peer review under the responsibility of editorial board of Environmental Functional Materials.

https://doi.org/10.1016/j.efmat.2024.12.004
Received 13 November 2024; Received in revised form 20 December 2024; Accepted 23 December 2024

1. Introduction

Surface water contamination caused by antibiotics such as tetracycline (TC), ciprofloxacin, amoxicillin and norfloxacin, have posed serious risks to the environment and human health. Among these antibiotics, TC, widely used in agriculture and animal husbandry, is persistently released into aquatic systems, leading to microbial resistance and ecological imbalances [1–3]. Given the challenges in treating antibiotic-laden wastewater, effective and sustainable treatment solutions are urgently needed. While methods such as adsorption, membrane separation, coagulation and biodegradation have been explored to remove TC from wastewater [4–6], problems such as high cost, low efficiency, and secondary pollution limit their practical application. Moreover, the variability in environmental conditions such as pH, temperature, and light intensity further complicates the efficiency of these methods [7,8].

Photocatalysis has garnered attention as a promising and eco-friendly solution for degrading organic pollutants under light irradiation [9]. However, achieving efficient photocatalysis under realistic environmental conditions remains a challenge, necessitating innovations in material design and functionality. Recently, researchers have found that heterojunctions with appropriate semiconductor materials can enhance photocatalytic performance by improving light utilization and electron (e^-) and hole (h^+) transfer [10,11]. The $Ag/Ag_2O/BiPO_4/Bi_2WO_6$ (Ag-BWO) heterojunction photocatalyst, in particular, offers visible-light-driven photocatalytic capabilities [12]. In this photocatalyst, the metallic Ag nanoparticles extend the visible light response range of Bi-based photocatalysts through surface plasmon resonance (SPR) under visible light irradiation, significantly enhancing photocatalytic efficiency [12]. Additionally, Ag_2O was promising visible-light-driven photocatalysts due to their narrow band gaps, enabling efficient utilization of solar energy. Furthermore, Ag-based semiconductors can combine with Bi_2WO_6 and $BiPO_4$ to form heterojunction structures [13,14]. These heterojunctions improve the separation of e^--h^+ pairs, reducing recombination rates and enhancing quantum efficiency. Overall, these properties make Ag-BWO an attractive photocatalyst for addressing organic pollutant degradation. However, to address the degradation of complex antibiotic like TC, further enhancement strategies are required, focusing on improving charge separation and catalytic redox capabilities.

In recent years, the introduction of Z-scheme heterojunction has presented a novel approach to boost photocatalytic redox capabilities [15–17]. In contrast to traditional heterojunctions, Z-scheme heterojunction formation can remove more complex and resistant organic matter by increasing photocatalysts' redox ability and enhancing photoinduced e^--h^+ separation efficiency [18,19]. Graphitic carbon nitride ($g\text{-}C_3N_4$) has been increasingly utilized in Z-scheme photocatalyst formation due to its optimal band gap and unique layered structure. Besides, $g\text{-}C_3N_4$ is characterized by its non-toxic nature, cost-effectiveness, ease of synthesis, commendable light absorption capacity, advanced optical properties, and thermal stability. In addition, its suitable valence potential (1.4 eV), promotes the generation of superoxide radicals ($\cdot O_2^-$) essential for effective oxidative degradation [20–22]. Exfoliation techniques allow the preparation of $g\text{-}C_3N_4$ nanosheets, which can be easily immobilized with Bi and Ag nanoparticles to improve the e^- interaction and photocatalytic performance [23]. Therefore, the advantages of introducing $g\text{-}C_3N_4$ well-suited for Z-scheme configurations that rely on the synergistic interaction of multiple semiconductor materials [24].

Despite recent progress, research on Z-scheme heterojunctions combining Ag-BWO with $g\text{-}C_3N_4$ for TC degradation remains limited. Additionally, optimizing the $g\text{-}C_3N_4$ ratio is crucial for ensuring a high crystallinity and mature structural growth, which are directly related to photocatalytic performance. By achieving an ideal interaction between Bi_2WO_6 and $BiPO_4$ components in Ag-BWO, the enhanced Z-scheme $Ag/Ag_2O/BiPO_4/Bi_2WO_6/g\text{-}C_3N_4$ (ABC) photocatalyst could facilitate effective TC degradation. This study systematically investigated the impact of $g\text{-}C_3N_4$ ratio on photocatalytic efficiency for TC degradation and explored the structural and optical properties of the developed ABC. Characterizations such as UV–vis, photocurrent, and EIS assessments shed light on its photoelectron-chemical properties, while XRD, FTIR, XPS, and TEM were employed to analyze the structure and morphology of ABC. Additionally, density functional theory (DFT) calculations identified vulnerable sites on the TC molecule, aiding in the degradation pathway analysis and toxicity assessments of intermediates. This research provides insights into developing high-efficiency Z-scheme photocatalysts for antibiotic degradation under diverse environmental conditions, suggesting a viable solution for sustainable wastewater treatment.

2. Materials and methods

2.1. Preparation of the photocatalysts

The $g\text{-}C_3N_4$ was synthesized by calcining 10 g of urea at 550 °C for 4.5 h with a heating rate of 5 °C/min. After cooling, the $g\text{-}C_3N_4$ powder was ground uniformly and pre-treated with sonication in isopropanol (IPA) as the solvent.

The $Ag/Ag_2O/BiPO_4/Bi_2WO_6/g\text{-}C_3N_4$ was synthesized through a two-step hydrothermal method with modifications. First, 45 mL of Na_2WO_4 solution (10 μmol) was combined with 15 mL of $Bi(NO_3)_3$ solution (20 μmol in 1 mol/L HNO_3) and stirred for 3 h at room temperature. The pH was adjusted to 7 using $NH_3{\cdot}H_2O$ before transferring the solution to a 100 mL Teflon-lined autoclave and heating at 160 °C for 18 h. After several washes with ethanol and water, the sample was resuspended in 45 mL ethanol. 2 μmol Ag^+ (Ag_3PO_4 and $AgNO_3$) and 0.14 μmol K_2HPO_4 were dissolved in 5 mL of 1 mol/L HNO_3 solution and then were added into the above mixture with 0.30 $g\text{-}C_3N_4$ ($ABC_{(10)}$), 0.12 $g\text{-}C_3N_4$ ($ABC_{(25)}$), 0.06 $g\text{-}C_3N_4$ ($ABC_{(50)}$) together, followed by 10-min sonification. This mixture was then reacted at 120 °C for 4 h, and the resulting precipitates were collected, washed with ultrapure water, and dried at 85 °C for 24 h to obtain the ABC powders. A control Ag-BWO composite was prepared following the same two-step hydrothermal process, excluding the addition of $g\text{-}C_3N_4$.

2.2. Evaluation of photocatalytic activity

The photocatalytic activity of the synthesized samples was assessed through TC degradation experiments under simulated solar light. For each test, 0.050 g of photocatalyst was dispersed in 50 mL of 10 mg/L TC aqueous solution, stirred in the dark for 1 h to achieve adsorption equilibrium, and then irradiated under simulated solar light (550 W/m^2) at 25 °C. Experiments were conducted in triplicate. Photocatalytic performance was evaluated comparatively, and degradation kinetics were analyzed using the Langmuir-Hinshelwood model:

$$-\ln\left(\frac{C_t}{C_0}\right) = kt \tag{1}$$

where k is the degradation rate constant (min^{-1}), t is the degradation time. Total organic Carbon (TOC) was examined with a TOC analyzer (TOC-5000A, Shimadzu, Kyoto, Japan).

2.3. Structural and photocatalytic characterization

The morphology of as-prepared photocatalysts was characterized by Scanning Electron Microscope (SEM) and energy dispersive X-Ray

spectroscopy (EDX) (FE-SEM (S-4800) + EDX, Hitachi) and Transmission Electron Microscopy (TEM) (JEOL JEM 2100F). The crystal phase was characterized by X-ray Diffraction (XRD) (RINT-Ultima III, Rigaku) with Cu Kα radiation (k = 1.54178 Å). The surface chemical environment was analyzed using the X-ray photoelectron spectroscopy (XPS) (JPS-9010TR, JEOL) and all the data were calibrated with C 1s binding energy of 284.8 eV. Fourier transform infrared (FTIR) spectra were obtained using an FTIR infrared spectrometer (FTIR-6800, JASCO) with KBr as the reference. UV–Vis diffuse reflectance spectra were obtained over a range of 300–700 nm (V-750, JASCO). The Brunauer-Emmett-Teller (BET) method was used for the determination of surface area by Beckman Coulter SA-3100. Photoelectrochemical performance, including electrochemical impedance spectroscopy (EIS) and photocurrent response, was measured with an Electrochemical Measurement System (HZ-7000, HOKUTO DENKO) using a platinum net as the counter electrode, a standard calomel reference electrode, ITO glass as the working electrode, and 1 mol/L Na_2SO_4 as the electrolyte. Photocurrent response was measured at 0.6 V.

2.4. Detection of reactive species and charge transfer mechanisms

To clarify the mechanism of TC degradation, radical trapping experiments were performed. For each experiment, 0.05 g of photocatalyst and 1 mM of a specific scavenger were added to 50 mL of 10 mg/L TC solution. Ethylenediaminetetraacetic acid (EDTA), IPA, and 1,4-benzoquinone were used as scavengers for h^+, hydroxyl radicals (•OH), and superoxide radicals ($\bullet O_2^-$), respectively. Electron spin resonance (ESR) spectroscopy was also conducted to detect the presence of h^+, $\bullet O_2^-$, and •OH under both light and dark conditions.

2.5. DFT calculation

Structural optimization and computational analyses of TC were conducted using Gaussian 16.0 under B3LYP/6-311G (d,2p) hybrid functional method, and analyzed by frequency recording to obtain the wave function of the stable structure. The frontier molecular orbitals (the highest occupied molecular orbits (HOMO), the lowest unoccupied molecular orbits (LUMO) and Fukui functions (the nucleophilic (f^+), electrophilic (f^-) and radical attack (f^0)) were then obtained and plotted by Multiwfn 3.8_dev and VMD (1.9.3 version) [25].

2.6. Intermediates analysis and toxicity assessment

TC and its intermediates concentrations were quantified using LC-QTOF/MS (Bruker compact LC-MS System)with the Electrospray ionization (ESI) as the ion resource. Chromatographic separation was performed on a C18 column with solution A: water phase (0.1 % formic acid) and solution B: organic phase (100 % MeCN) with a gradient elution from 5 % to 95 % MeCN for 10 min at a flow rate of 0.5 mL/min, by applying the following linear gradient: 0 min 1 % B, 4 min 10 % B, 11.50 min 20 % B, 13 min 30 % B, 15 min 45 % B, 18 min 50 % B, 23 min 1 % B, 28 min 1 % B. The injection volume was 20 μL, and the oven temperature was set to 25 °C. Detection wavelength was set to 270 nm. With the results from LC-QTOF/MS, the environmental toxicity of TC and its degradation intermediates were simulated by quantitative structure-activity relationship (QSAR) method by applying the Toxicity Estimation Software Tool (T.E.S.T.) developed by EPA [26].

3. Results and discussion

3.1. Performance of optimized g-C_3N_4 mass ratio composite and its environmental adaptability

Fig. 1a illustrated the photocatalytic performances of various g-C_3N_4 mass ratio composite, Ag-BWO, and g-C_3N_4 for TC degradation. Among these photocatalysts, $ABC_{(25)}$ demonstrated the highest adsorption and photocatalytic activity, achieving a degradation efficiency up to 96.8 % within 60 min. Additionally, as shown in Fig. 1b, $ABC_{(25)}$ exhibited the highest k of 0.0525 min^{-1} compared to the other g-C_3N_4-based samples. In addition, TOC was further conducted to clarify the mineralization rate of TC (Fig. 1c). After 60 min of photocatalytic degradation process,

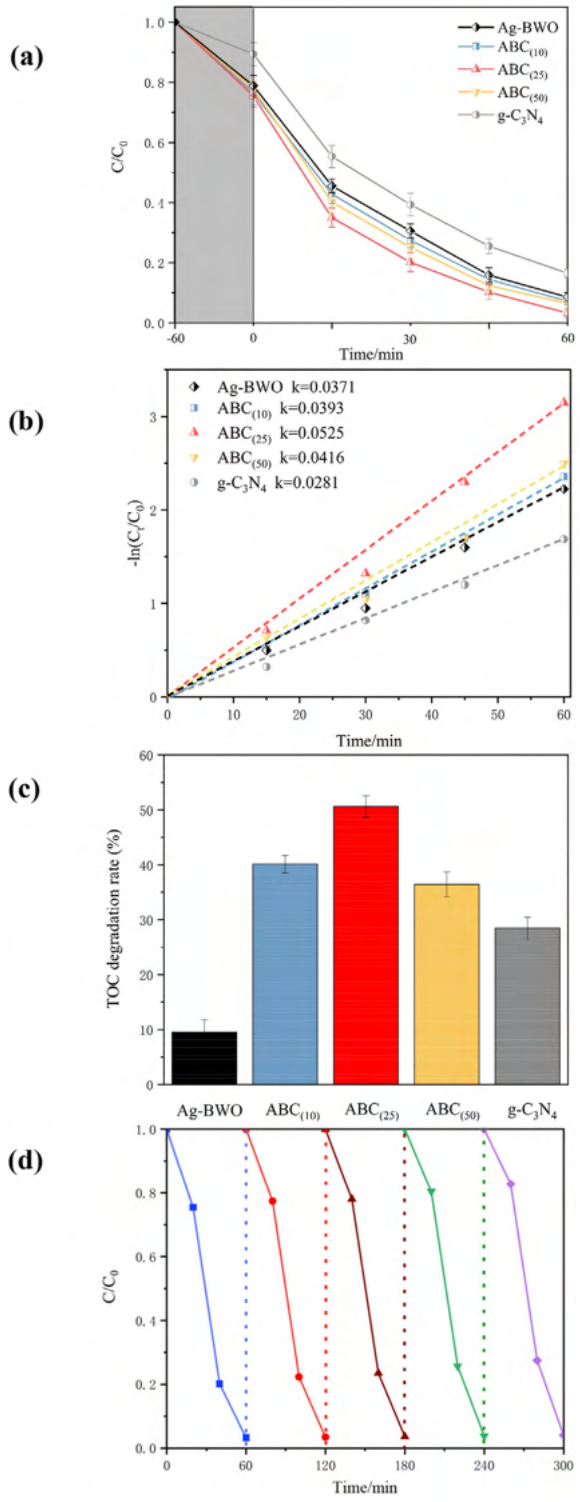

Fig. 1. Photocatalytic degradation of tetracycline. (a) Degradation efficiency, (b) first-order kinetic plot, (c) total organic carbon (TOC) degradation rate and (d) cyclic degradation performance of $ABC_{(25)}$. (Irradiation intensity: 550 W/m^2, tetracycline concentration: 10 mg/L, pH = 7, Tetracycline absorption peak: 357 nm).

$ABC_{(25)}$ showed the best mineralization performance of 51.6 %, which was superior to other composites. Comparing to the other suboptimal composites ($ABC_{(10)}$ and $ABC_{(50)}$), as well as the single loading of Ag-BWO and g-C_3N_4, the enhanced degradation efficiency of $ABC_{(25)}$ was probably attributed to the most advantageous g-C_3N_4 mass ratio, which may form an ideal interaction between Bi_2WO_6 and $BiPO_4$. This configuration promoted the generation of reactive species under solar light, thus facilitating TC removal. Table S1 showed the recent publications on degradation of TC by Bi_2WO_6-based photocatalysts. Compared with most reports, the developed $ABC_{(25)}$ sample exhibited the highest degradation efficiency to TC, which was about 1.75–3.88 times higher than other reports [27–30]. Furthermore, recycled experiments were conducted to clarify the stability and reusability of synthesized $ABC_{(25)}$ photocatalyst. As shown in Fig. 1d, the $ABC_{(25)}$ maintained high photocatalytic activity above 96.0 % after 5 cycles. Herein, the synthesized $ABC_{(25)}$ photocatalyst showed significant promise for effective and sustainable TC pollution treatment.

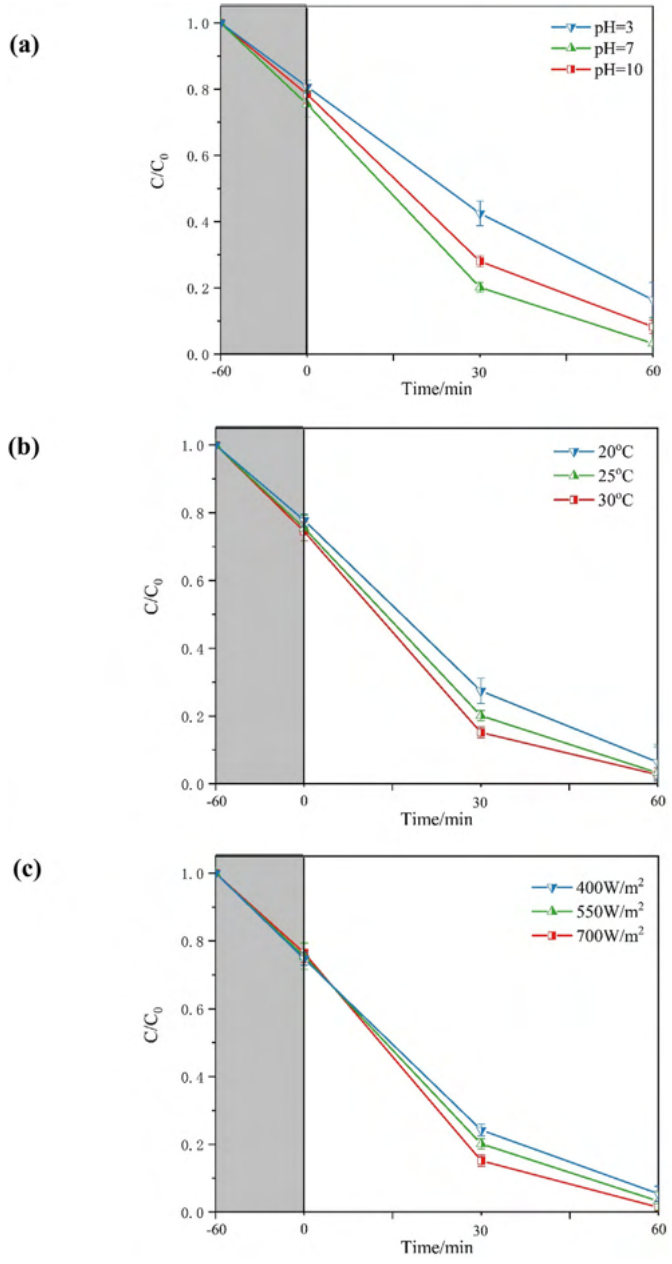

Fig. 2. Influence of environmental factors on TC degradation with $ABC_{(25)}$. (a) pH, (b) temperature, and (c) light irradiation density.

In light of its superior TC degradation ability, the potential of the $ABC_{(25)}$ composite for wastewater treatment was further explored by evaluating its performance under various environmental conditions, including pH, temperature, and light intensity.

The effects of initial pH on the photocatalytic treatment of TC in water was presented in Fig. 2a. $ABC_{(25)}$ exhibited the highest degradation efficiency at a neutral pH of 7 under solar light. While it relatively declined in both acidic and alkaline conditions. The observed degradation results could be ascribed to the different ionic states of TC at varying pH levels. The dissociation constants of TC are 3.32, 7.68, and 9.68 [31], indicating that TC exists in distinct ionic forms across different pH level range. Below pH 3.32, TC is predominantly in its cationic form (TCH_3^+), reducing its ability to react with radicals due to H^+ consumption. Above pH 9.68, TC becomes an anion (TCH^- or TC_2^-), resulting in electrostatic repulsion and poor adsorption on the negatively charged photocatalyst surface. Between pH 3.32 and 7.68, TC exists as a zwitterion ($TCH_2^\pm$), allowing optimal degradation without competitive reactions or electrostatic issues, consistent with theoretical analysis [32]. The results indicated that $ABC_{(25)}$ was effective for TC degradation across a wide pH range from 3 to 10, and suitable under the neutral pH condition. This aligns well with the pH of most real-world pollutant environments [33, 34], demonstrating its strong environmental adaptability.

The influence of temperature on the degradation of TC under solar light is presented in Fig. 2b. The results showed that the photocatalytic removal efficiency of TC increases as the temperature raised from 20 °C to 30 °C. At higher temperatures (30 °C), e^--h^+ recombination is reduced, leading to a greater generation of radical species with higher oxidative potential, promoting the TC decomposition. Even at the lower temperature of 20 °C, the degradation efficiency remained significant under solar light. In natural environments, the actual water temperature typically ranges from 20 °C to 30 °C, depending on geographical location, season, and weather conditions [35]. This temperature range aligns with the experimental conditions in this study, further supporting the applicability of $ABC_{(25)}$ for real-world water treatment scenarios.

The effect of light intensity on the photocatalytic efficiency of $ABC_{(25)}$ is shown in Fig. 2c. The results clearly indicated that TC degradation efficiency increased proportionally with light intensity, ranging from 400 to 700 W/m^2. Specifically, the TC degradation rates at 400, 550, and 700 W/m^2 were 94.9 %, 96.7 %, and 99.7 %, respectively. The enhanced photocatalytic performance at higher light intensity (700 W/m^2) can be attributed to the increased generation of excited e^- and h^+ on the photocatalyst surface. Even at lower light intensity (400 W/m^2), the TC degradation efficiency remained high, demonstrating the strong redox capability of ABC under low-light conditions. Typically, natural light intensity is around 550 W/m^2, further supporting the applicability of these findings in real water conditions [36]. Therefore, the photocatalytic degradation ratio was positively correlated with the incident light irradiation intensity, which is fit for the degradation results. All these results concerning about environmental factors highlighted the robust degradation performance of $ABC_{(25)}$ consistently exhibited across a variety of typical environmental conditions, making it applicable for real-world utilization.

3.2. *Optical and photoelectron-chemical performance*

In order to understand the reasons behind the superior photocatalytic performance of the optimized $ABC_{(25)}$, systematic characterization methods including light absorption, charge recombination, e^- transfer, and photocurrent analysis were employed. As illustrated in Fig. 3a, the UV–Vis spectrum of $ABC_{(25)}$ showed the highest absorption intensity. Notably, $ABC_{(25)}$ exhibited an increasing absorption peak from 450 nm to 600 nm, with a marginal redshift towards longer wavelengths. On the other hand, $ABC_{(10)}$ showed reduced absorption due to excessive g-C_3N_4 loading, which hindered the growth and development of the Bi_2WO_6 base material. Similarly, $ABC_{(50)}$ showed lower visible light absorption, indicating that lower amounts of g-C_3N_4 showed no significant improved

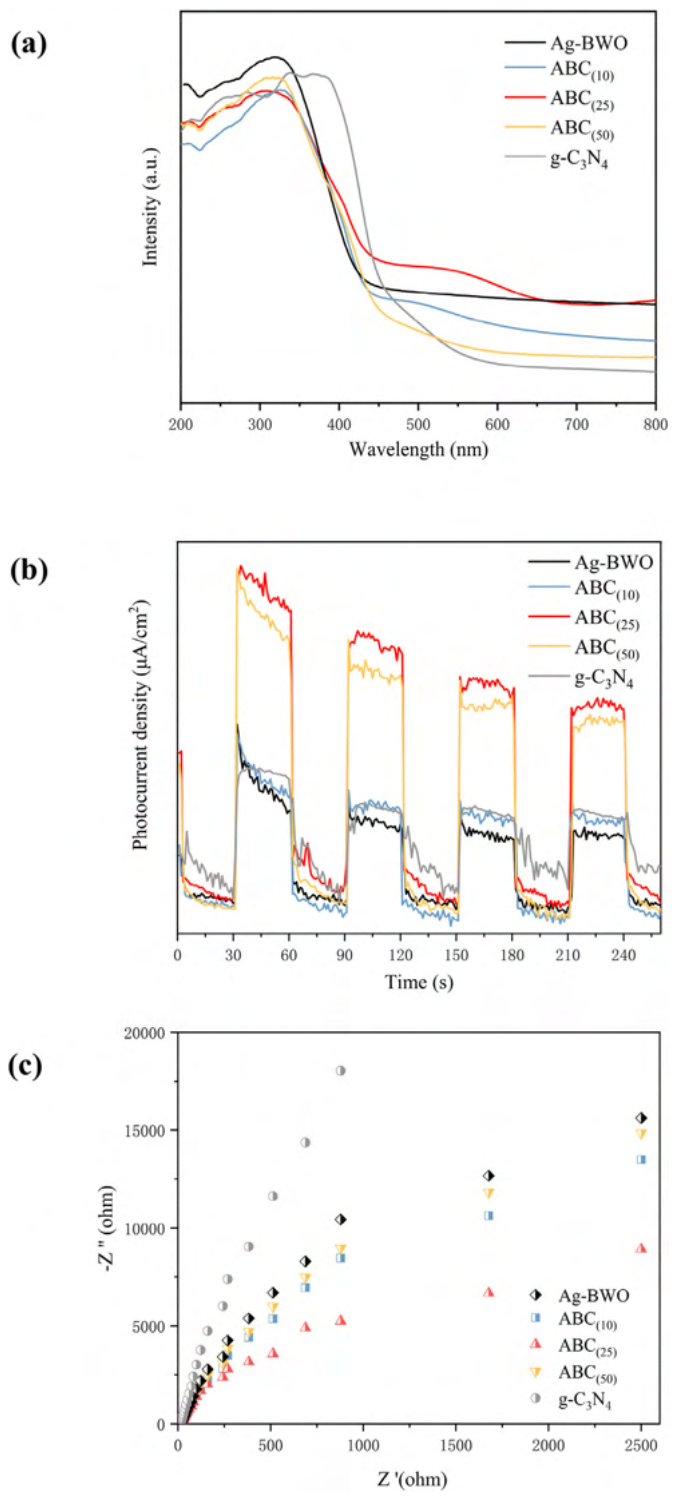

Fig. 3. (a) UV–Vis absorption spectra, (b) photocurrent density, and (c) EIS spectra of different mass ratios of ABC, Ag-BWO and g-C_3N_4.

effect compared with the optimized $ABC_{(25)}$ These pronounced redshifts arose from the charge-transfer transition between g-C_3N_4 and Ag-BWO, facilitating the efficient transferring ability of solar energy. Furthermore, the band gap energy (E_g) of the composites was calculated using the equation $E_g = 1240/\lambda_g$ (eV) [37], where λ_g represents the absorption edge derived from the intersection between the tangent of the absorption curve and the abscissa. As shown in Table S2, the E_g of g-C_3N_4, Ag-BWO, $ABC_{(10)}$, $ABC_{(25)}$, and $ABC_{(50)}$ are 2.62, 2.70, 2.61, 2.30, 2.48eV, respectively. The lowest band gap of $ABC_{(25)}$ signified the enhanced the utilization of visible light due to the incorporation of g-C_3N_4, thereby leading to the improved the efficacy of photocatalytic reactions.

Additionally, the photocatalytic properties of ABC composites were detected through the conduction of transient photocurrent responses and EIS. As shown in Fig. 3b, the photocurrent densities of the as-synthesized catalysts exhibited rapid increases and sharp decreases upon switching the light on and off, respectively, indicating their outstanding photo-responsive abilities [38–40]. Typically, $ABC_{(25)}$ achieved the highest transient photocurrent density, which was associated with the longest charge pair lifetime, indicating excellent photocatalytic activity. $ABC_{(10)}$ exhibited a similar photocurrent density to g-C_3N_4, suggesting that a lower ratio of g-C_3N_4 negligibly affects the charge transfer. On the other hand, $ABC_{(50)}$ showed a lower photocurrent density compared to $ABC_{(25)}$, which may be attributed to the excessive modification of g-C_3N_4. The pure Ag-BWO composite exhibited a weaker photocurrent responsivity to visible light and faster charge recombination. In comparison, all the ABC composites demonstrated enhanced photocurrent intensities, evidencing the improvement of e^- chemical properties by introducing g-C_3N_4. Notably, the average photocurrent intensity of $ABC_{(25)}$ was about twice as that of Ag-BWO. These findings suggested that the optimized ratio of g-C_3N_4 in $ABC_{(25)}$ may promote the effective growth of photocatalyst with higher crystallinity. This enhancement resulted in more effectively separated photo-generated e^--h^+ pairs, thereby leading to the improved photocatalytic performance [41]. In Fig. 3c, the semicircle radius of $ABC_{(25)}$ was smaller than the $ABC_{(10)}$ and $ABC_{(50)}$ composites. Normally, EIS arc possessing a significantly smaller radius indicates a lower charge-transfer resistance during the photocatalytic process [42]. $ABC_{(25)}$ with a smaller radius indicated a reduced interface resistance for carrier transfer, which resulted from the enhanced electron mobility, While $ABC_{(10)}$ and $ABC_{(50)}$ exhibited higher interface resistance and lower e^- mobility compared to $ABC_{(25)}$. These results consistent with the photocurrent results highlighted that the optimized $ABC_{(25)}$ exhibited the proper optical and photoelectron-chemical performance.

3.3. Structure and morphology analysis

To further investigate the performance disparity of the different g-C_3N_4 ratios, characterizations of their crystal structures and composition components were enforced. The crystal phases and functional groups of the photocatalysts were analyzed by XRD and FTIR (Fig. 4). For pure g-C_3N_4, a distinct higher diffraction peak was detected around 27.4° (Fig. 4a), which was indexed to (0 0 2) plane (JCPDS No. 87–1526) [43]. The diffraction peaks at 28.3°, 32.8°, 47.0°, 55.8° and 58.5° in Ag-BWO and all the ABC samples belonged to (1 3 1), (2 0 0), (2 0 2), (3 3 1) and (2 6 2) planes of Bi_2WO_6, respectively (JCPDS No.39-0256) [44]. However, no characteristic peaks of g-C_3N_4 were observed in all the ABC samples, likely due to the overlap between peaks of Bi_2WO_6 and g-C_3N_4. In addition, no other diffraction peaks were found, indicating the high purity of the prepared photocatalysts [22]. Furthermore, the XRD patterns were used to calculate the crystallite size of the as-prepared samples. Among the samples, $ABC_{(25)}$ exhibited the largest crystallite size of 26.3 nm, while $ABC_{(10)}$ (17.4 nm), $ABC_{(50)}$ (12.0 nm), Ag-BWO (17.6 nm), and g-C_3N_4 (3.7 nm) showed smaller sizes (Table S3). This result suggested that the $ABC_{(25)}$ exhibited the highest phase purity and the most mature crystal structure.

Further characterizations were conducted through FTIR analysis (Fig. 4b). The peak observed around 810 cm^{-1} in the ABC samples was attributed to the vibration of s-triazine units, a signature of g-C_3N_4, while peaks between 1200 and 1800 cm^{-1} corresponded to the stretching of C-N or C=N bonds [45]. The broad peak between 3000 and 3500 cm^{-1} was ascribed to the stretching vibration of N-H or O-H. In the spectra of ABC, the characteristic peaks at 590 cm^{-1} and 730 cm^{-1} were attributed to stretching vibrations of Bi-O and W-O bands, indicating the presence of Bi_2WO_6 in ABC. The peak around 1380 cm^{-1} could be explained by the characteristic vibration of P=O band in $BiPO_4$. Notably, each

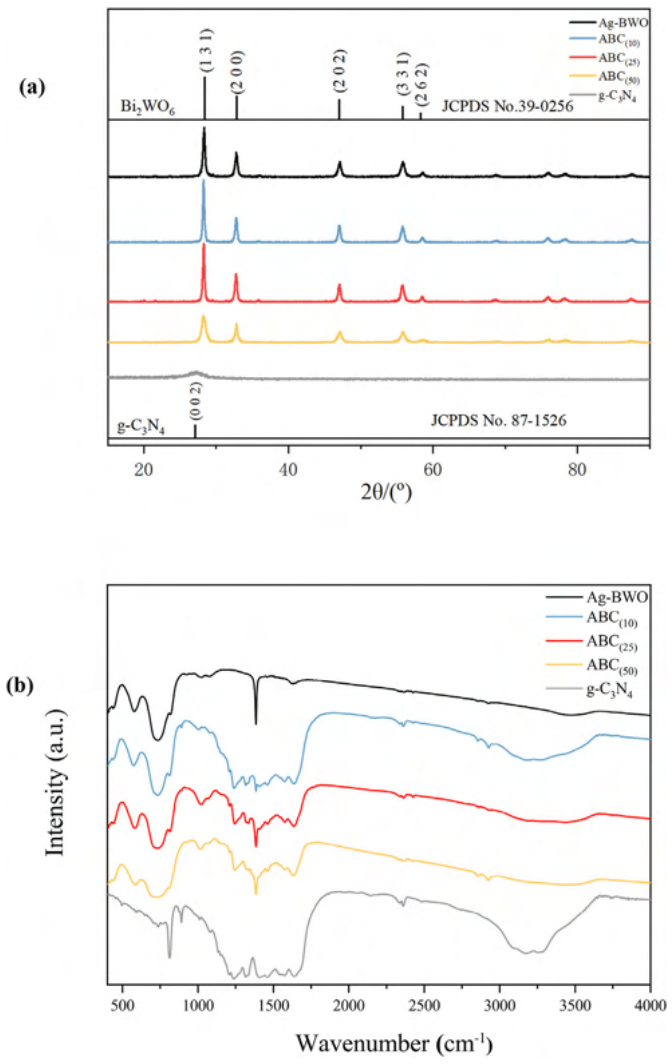

Fig. 4. (a) XRD patterns, and (b) FTIR spectra of different mass ratio of ABC, Ag-BWO and g-C_3N_4.

characteristic peak observed in ABC samples originated from Ag-BWO and g-C_3N_4, providing partial evidence for the successful modification of g-C_3N_4 into Ag-BWO. Additionally, shifts existed in the C-N and C=N peaks (1200~1800 cm^{-1}) in ABC, compared to pure g-C_3N_4 (1000~1800 cm^{-1}) [46], suggested the interaction between the g-C_3N_4 and other components in the ABC composite. Consequently, the XRD and FTIR results indicated the successful synthetization of ABC.

Furthermore, the morphology of the synthesized photocatalysts was visualized by SEM and TEM. As shown in the SEM image (Fig. 5a), the g-C3N4 displayed an irregular flake structure, while Ag-BWO exhibited a multi-layered sheet-like structure, which was consistent with previous studies [47]. Upon modifying g-C_3N_4 into Ag-BWO, the Ag-BWO were randomly distributed over the g-C_3N_4 nanosheets, resulting in the formation of irregularly stacked sheets. Additionally, TEM image (Fig. 5b) provided a clear visualization of the ABC morphology, revealing a tight contact between g-C_3N_4 and Ag-BWO. Furthermore, the TEM analysis declared the observation of crystal lattice parameters of approximately 0.334 nm, 0.347 nm, 0.235 nm, 0.236 nm, corresponding to (1 3 1) plane of Bi_2WO_6, (0 2 0) plane of $BiPO_4$, (1 1 1) plane of Ag and (2 0 0) plane of Ag_2O, respectively [48,49]. These findings further confirmed the successful construction of the ABC composite, as corroborated by the FTIR data. Moreover, the EDX mapping in Fig. 5c indicated a homogeneous distribution of elements including C, N, Ag, O, Bi, P and W in the ABC composite, further supporting the successful synthesis of the g-C_3N_4 modified Ag-BWO composite.

To gain further insight into the surface elemental composition and chemical states of the photocatalysts, XPS analysis was carried out. As shown in Fig. 6, the XPS spectra of ABC proved the existence of C, N, O, Ag, Bi, and W elements, which are consistent with the EDX results. The high resolution of C 1s spectra (Fig. 6a) exhibited two peaks at approximately 284.5 and 288.2 eV, corresponding to ubiquitous carbon contamination and sp^2 hybridized carbon in aromatic rings [50]. In Fig. 6b, two distinct peaks at 398.4 and 399.7 eV were observed, which can be attributed to sp^2-bonded N atoms in C-N-C and tertiary N atoms in N-$(C)_3$, respectively. In addition, a weak peak at 404.8 eV, assigned to π-excitations, was detected in all ABC samples, indicating the interaction between Ag-BWO and g-C_3N_4 through the π-electrons of g-C_3N_4 heterocycles [51,52]. The O 1s spectra (Fig. 6c) showed peaks at 529.5, 530.8, 531.1, and 533.3 eV, representing W-O or Ag-O, Bi-O, P-O in the composite, respectively [53]. Furthermore, peaks at 374.1 and 367.9 eV (Fig. 6d) belonging to Ag 3d were attributed to the binding energies of Ag $3d_{3/2}$ and Ag $3d_{5/2}$, demonstrating the Ag^0 and Ag^+ state in ABC [54]. Moreover, two peaks at 164.9 and 159.8 eV (Fig. 6e), corresponded to Bi $4f_{5/2}$ and Bi $4f_{7/2}$, respectively, indicating a state of Bi^{3+} [55]. Moreover, the patterns of W 4f showed peaks at 37.7 and 35.9 eV (Fig. 6f), which were ascribed to W $4f_{5/2}$ and W $4f_{7/2}$, respectively [56]. In conclusion, based on the characterization of XRD, FTIR, SEM and TEM images, EDX mapping and XPS spectra, it could be confirmed that with g-C_3N_4 effectively incorporated into the Ag-BWO structure, the ABC composite was successfully constructed.

Moreover, a comprehensive analysis of BET surface area and pore size distribution for g-C_3N_4, Ag-BWO, and $ABC_{(25)}$ was conducted to clarify their structural characteristics and their relationship with photocatalytic properties. The N_2 adsorption-desorption isotherms for all samples are characterized as type IV with H3 hysteresis loops, indicating the presence of mesoporous structures. The results of the BET surface area analysis revealed that $ABC_{(25)}$ exhibits the highest surface area of 22.524 m^2/g, followed by Ag-BWO with 12.041 m^2/g, and g-C_3N_4 with the lowest surface area of 6.331 m^2/g (Fig. S1a). A higher surface area facilitates greater adsorption of reactant molecules, which is beneficial for enhancing photocatalytic efficiency [12]. Additionally, the pore size distribution (Fig. S1b) demonstrated that $ABC_{(25)}$ has a broader pore size range and a higher total pore volume compared to Ag-BWO and g-C_3N_4. This feature further supported the photocatalytic performance of $ABC_{(25)}$ due to improved adsorption for reactants and products. In summary, the higher specific surface area and well-developed mesoporous structure of $ABC_{(25)}$ contribute to its enhanced photocatalytic performance in more efficient light absorption, greater surface reactivity, and improved charge carrier dynamics.

3.4. Z-scheme mechanisms of ABC photocatalyst

According to the above results, inducing an optimized mass ratio of g-C_3N_4 into Ag-BWO leads to excellent photocatalytic activity for the degradation of TC, as well as improved crystallinity and accelerated charge carrier transfer. To further elucidate the mechanism of TC photodegradation by $ABC_{(25)}$, radical trapping experiments and ESR spectra were conducted to identify the active species involved in the photocatalytic process. EDTA, IPA and 1–4 benzoquinone were used as the scavengers of h^+, •OH and $•O_2^-$, respectively [57]. As shown in Fig. 7a, compared to TC degradation by $ABC_{(25)}$ without scavengers, the photocatalytic activity decreased significantly in the presence of all three scavengers. Specifically (Fig. 7b), after 60 min of irradiation, the degradation rates were 70 %, 85 %, and 62 % with EDTA, IPA, and 1, 4-benzoquinone, respectively. The lowest degradation rate with 1,4-benzoquinone indicated that $•O_2^-$ was the primary active species in the photocatalytic process of $ABC_{(25)}$. Additionally, h^+ and •OH contributed to the reaction, with the order of active species effectiveness following $•O_2^- > h^+ >$ •OH. To further confirm the generation of active species in $ABC_{(25)}$, DMPO was employed in ESR analysis. Notably, the DMPO-$•O_2^-$

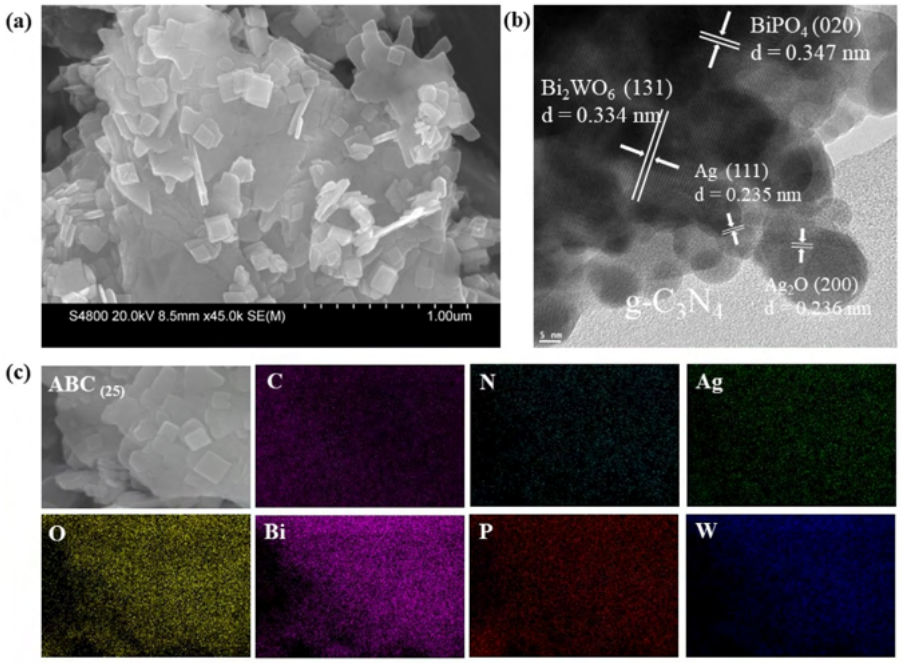

Fig. 5. (a) SEM image, (b) HRTEM image, and (c) EDX elemental mapping of $ABC_{(25)}$ composite.

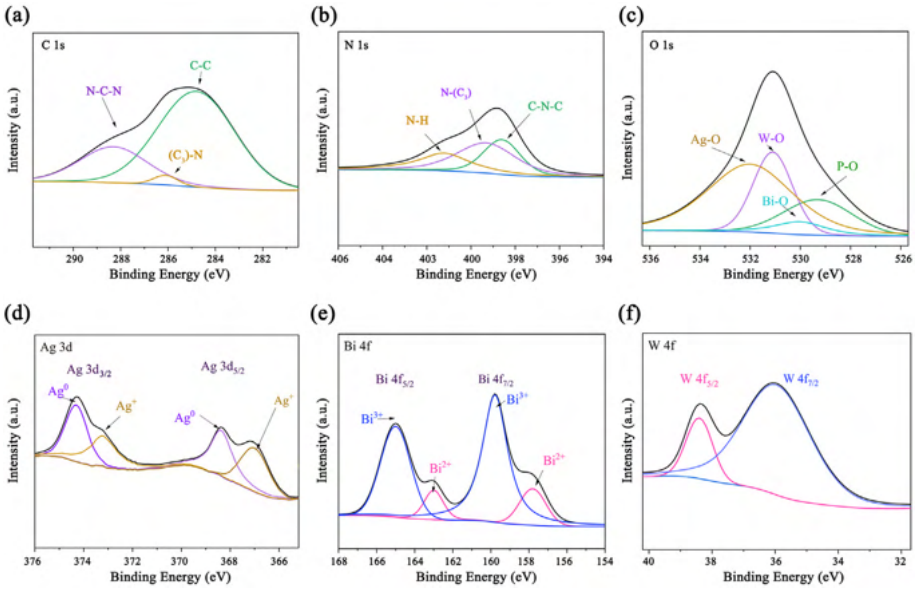

Fig. 6. XPS spectra of (a) C 1s, (b) N 1s, (c) O 1s, (d) Ag 3d, (e) Bi 4f and (f)W 4f of $ABC_{(25)}$ composite.

and DMPO-•OH signals were quantified under light irradiation in the photocatalyst composites, as shown in Fig. 7c and d. The DMPO-$•O_2^-$ signal increased significantly after 15 and 30 min of light exposure, confirming the generation of superoxide radicals during the photocatalytic process. Similarly, the DMPO-•OH signal showed a clear rise under light conditions, reflecting the active participation of hydroxyl radicals. No detectable signals were observed in the dark, indicating the light-driven property of the radical generation. These results highlight that $•O_2^-$, h^+, and •OH are the primary active species driving the photocatalytic degradation process of $ABC_{(25)}$, thereby contributing to its enhanced redox species inactivation performance.

The Mott-Schottky analysis was conducted to explore the band structure of $ABC_{(25)}$. As illustrated in Fig. 7e, the positive slopes of the Mott-Schottky plots confirm that $ABC_{(25)}$ exhibits n-type semiconductor characteristics [58,59]. Generally, the CB level of an n-type semiconductor is more about 0.1 eV negative than that of flat band potential. Thus, the CB level of $ABC_{(25)}$ was estimated to be −0.60 V vs. NHE (Fig. 7e). Regarding the calculation $E_{CB} = E_{VB}$-E_g and E_g value according to UV–VIS-DRS, VB level of $ABC_{(25)}$ was calculated to be +1.70 V vs. NHE. The oxidative ability of the photogenerated holes is closely related to their valence band position, while positive VB position is beneficial to oxidation reaction. VB potential of $ABC_{(25)}$ (+1.7 V vs. NHE) shows more positive than the water oxidation level (+1.23 V vs. NHE), indicating a highly capable of oxidizing H_2O to O_2. CB position of −0.60 V vs. NHE suggests the producing of O_2/$•O_2$- (−0.33 V vs. NHE) by $ABC_{(25)}$.

Based on the band structure analysis and scavenger results, a possible photocatalytic mechanism for the charge transfer of ABC under simulated solar light was proposed in Fig. 8. When exposed to solar light, the

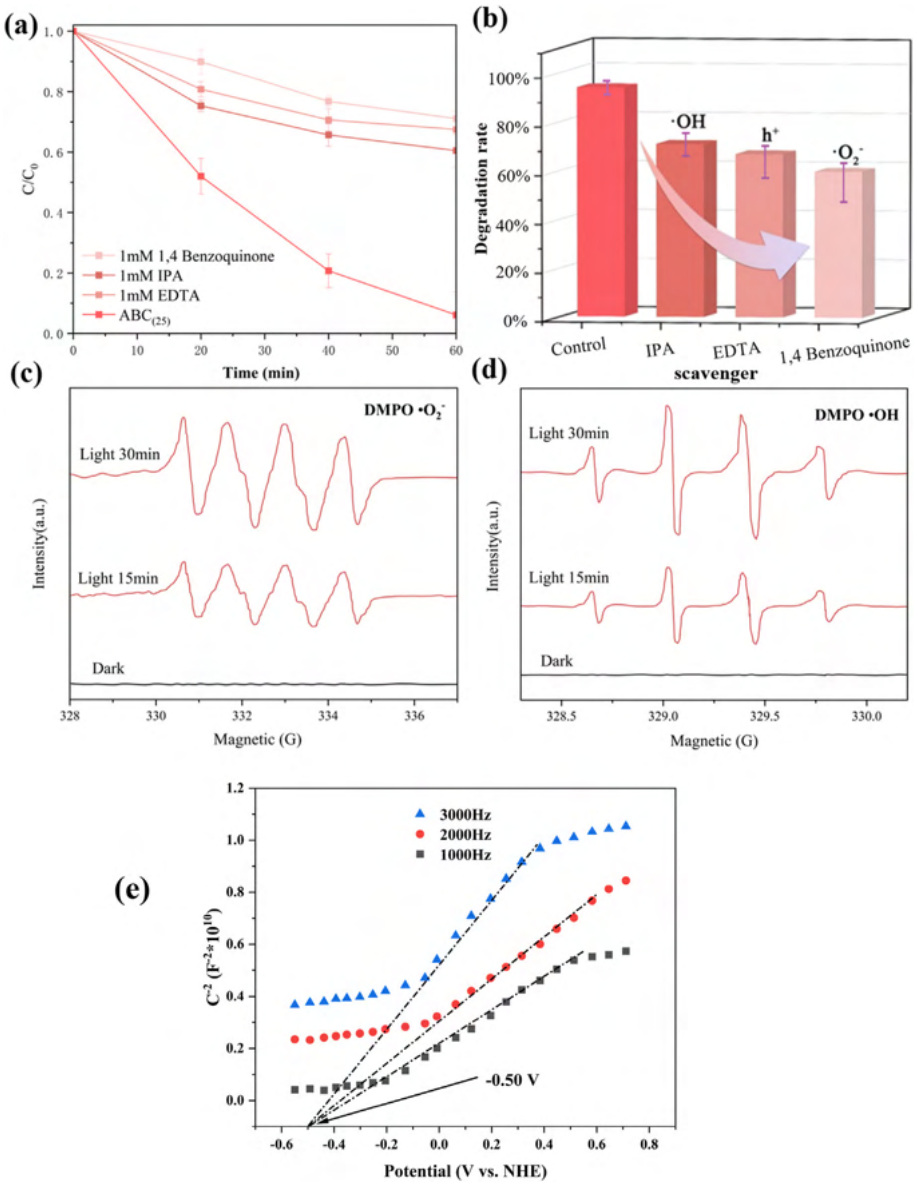

Fig. 7. (a, b) Radical trapping experiment for tetracycline degradation on $ABC_{(25)}$ with different scavengers, (c) ESR spectra of radical adducts trapped by DMPO-•O_2^- and (d) ESR spectra of radical adducts trapped by DMPO-•OH. (e) Mott−Schottky plots on $ABC_{(25)}$ with different frequency.

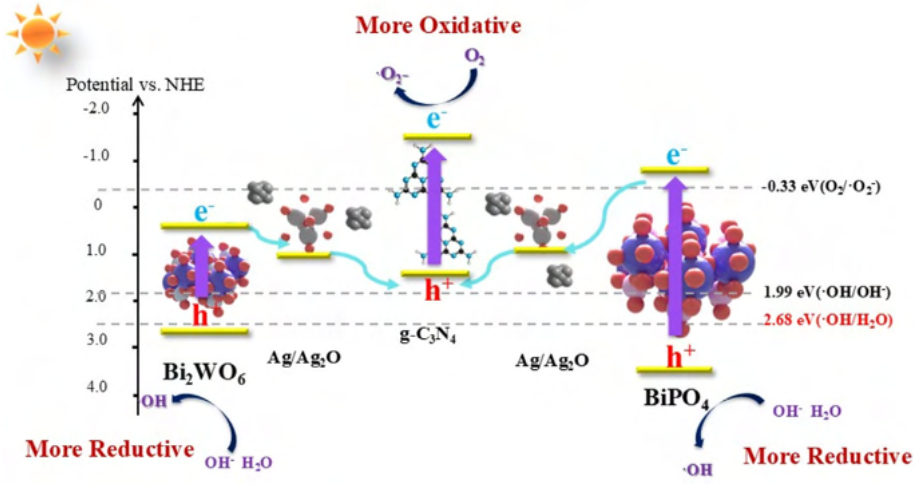

Fig. 8. The proposed schematic for the photocatalytic mechanism of $ABC_{(25)}$ composite.

photocatalysts absorb sufficient energy, causing e^- in the valence bands (VB) of Bi_2WO_6, Ag-Ag_2O, g-C_3N_4 and $BiPO_4$ to become excited and move to their respective conduction bands (CB), leaving h^+ in the VB. Since the CB potentials of g-C_3N_4 (−1.3 eV vs. NHE), Bi_2WO_6 (0.48 eV vs. NHE), $BiPO_4$ (−0.64 eV vs. NHE) and Ag_2O (0.2 eV vs. NHE) are more negative than the Fermi level of Ag (0.99 eV vs. NHE), the photogenerated e^- in their CBs can readily transfer to the Ag and Ag_2O nanoparticles, facilitating effective charge carrier separation [60]. Furthermore, due to the more negative CB potentials of $BiPO_4$ (−0.64 eV vs. NHE) and g-C_3N_4 (−1.3 eV vs. NHE) relative to the reduction potential of $O_2/\bullet O_2^-$ (−0.33 eV vs. NHE), e^- in the CB of $BiPO_4$ and g-C_3N_4 can react with O_2 to generate $\bullet O_2^-$, as confirmed by radical trapping experiments and ESR spectroscopy. Meanwhile, h^+ from the VB of Bi_2WO_6 and $BiPO_4$ can transfer to the VB of g-C_3N_4 and Ag_2O, owing to the more positive VB potential of Bi_2WO_6 (3.26 eV vs. NHE) and $BiPO_4$ (3.24 eV vs. NHE) compared to those of g-C_3N_4 (1.4 eV vs. NHE) and Ag_2O (1.4 eV vs. NHE). Recent studies indicate that a Z-scheme charge transfer pathway is feasible for g-C_3N_4-modified materials [61]. In this Z-scheme system, Ag-Ag_2O served as an e^- mediator, facilitating e^- transfer and recombination between photogenerated e^- from the CB of Ag_2O and h^+ from the VB of g-C_3N_4. Additionally, due to the potential difference between the CB of Ag_2O and the Fermi level of Ag, e^- accumulating in the CB of Ag_2O can easily transfer to Ag and subsequently recombine with h^+ from the VB of Ag_2O. Due to the effect of e^- mediator of Ag-Ag_2O, the e^- on the CB of $BiPO_4$ and Bi_2WO_6 could transfer to Ag-Ag_2O and recombine with h^+ from the VB of g-C_3N_4, accelerating efficient charge separation of different components. The formation of •OH radicals occurred due to the suitable redox potential of $\bullet OH/H_2O$ (2.68 eV vs. NHE), as verified by scavenger experiments and ESR spectroscopy.

In summary, e^- generated in the CB of $BiPO_4$ and Bi_2WO_6 transfer to Ag-Ag_2O, where they recombined with h^+ from the VB of g-C_3N_4. Remaining e^- in the CB of g-C_3N_4 react with O_2 to form $\bullet O_2^-$, while residual h^+ in the VB of $BiPO_4$ and Bi_2WO_6 oxidize H_2O or OH^- to produce •OH. Additionally, h^+ remaining in the VB of $BiPO_4$ and Bi_2WO_6 contribute to reductive reactions. These reactive species collectively drove the degradation process. Therefore, introducing g-C_3N_4 to Ag-BWO to form a Z-scheme system can significantly enhance light utilization, promote charge separation and transfer, and improve redox capacity. Based on the results above, the proposed reaction mechanism of ABC degradation on TC could be summarized as reactions (2)–(6), as follows:

$$ABC_{(25)} + \text{visible light} \rightarrow e^- + h^+ \quad (2)$$

$$(e^-) + \text{Ag-}Ag_2O \rightarrow \text{Ag-}Ag_2O\ (e^-) \quad (3)$$

$$\text{g-}C_3N_4\ (h^+) + \text{Ag-}Ag_2O\ (e^-) \rightarrow \text{Ag-}Ag_2O + \text{Energy} \quad (4)$$

$$(e^-) + O_2 \rightarrow \bullet O_2^- \quad (5)$$

$$(h^+) + H_2O/OH^- \rightarrow H_2O + \bullet OH \quad (6)$$

3.5. DFT calculations and reaction site prediction intermediates degradation pathway

In addition to the photocatalytic mechanism, understanding the degradation pathway is crucial for the photocatalytic removal of TC. Here, the frontier orbitals and Fukui Index of TC were computed using DFT calculations to elucidate the possible degradation pathway. Structurally, TC comprises a quadra-ring framework, which includes a benzene ring, a ketone group, and an enol group. The optimized HOMO and LUMO orbitals of TC are shown in Fig. 9a and b, highlighting its photostability and resistance to self-degradation. The HOMO is primarily localized on the benzene ring, while the LUMO is concentrated on a ketone group and an enol group. According to frontier orbital theory, atoms with higher LUMO components are more susceptible to nucleophilic reactions, while those with higher HOMO components tend to undergo electrophilic reactions [62]. Based on the LUMO and HOMO distributions, the Fukui function was applied to predict the nucleophilic and electrophilic sites (Fig. 9c–e). Atoms with higher f^+ values are more prone to nucleophilic attack by $\bullet O_2^-$. While atoms with elevated f^- values are more susceptible to electrophilic attack by h^+. Similarly, atoms with higher f^0 values are more vulnerable to free radical attack by •OH. In Table S4 and Fig. 9c, atoms 22 (O), 17 (C) and 15 (C) show the highest f^+ values (0.1075 0.0937 and 0.0893, respectively), indicating that the [-$N(CH_3)_2$] group is particularly venerable to nucleophilic attack by active species in the dismember process. The highest f^0 and f^- value are found at 20 (O) position with an iso-surface intensity of 0.108 (Table S4), indicating that the C=O bond is particularly prone to electrophilic attack by h^+ (Fig. 9d and e). The combined results of radical trapping experiments and Fukui function analysis suggested that nucleophilic attack is more likely to occur than electrophilic or free radical attack, supporting a stepwise degradation pathway for TC.

3.6. Intermediates degradation pathway and toxicity assessment

LC-MS analysis was performed to elucidate the step-by-step pathways for the photocatalytic degradation of TC, revealing a diverse array of intermediate products. Based on the identification of these intermediates by LC-MS, the proposed structures of the TC degradation products are presented in Table S5, and the degradation pathways are delineated in Fig. 10. Initially, nucleophilic sites in the TC molecule were attacked, leading to deamination and subsequent nucleophilic reactions, forming intermediates P1 (m/z = 428) and P2 (m/z = 396). Following this,

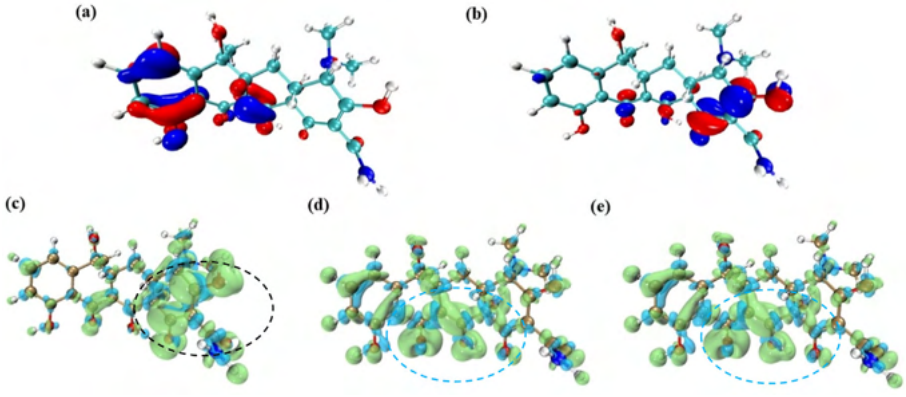

Fig. 9. The frontier molecular orbitals (a) HOMO, (b) LUMO, (c) nucleophilic attack sites (f^+), (d) electrophilic attack sites (f^-), and (e) radical attack sites (f^0) with optimized structure of tetracycline under B3LYP/6-311G (d,2p) methods.

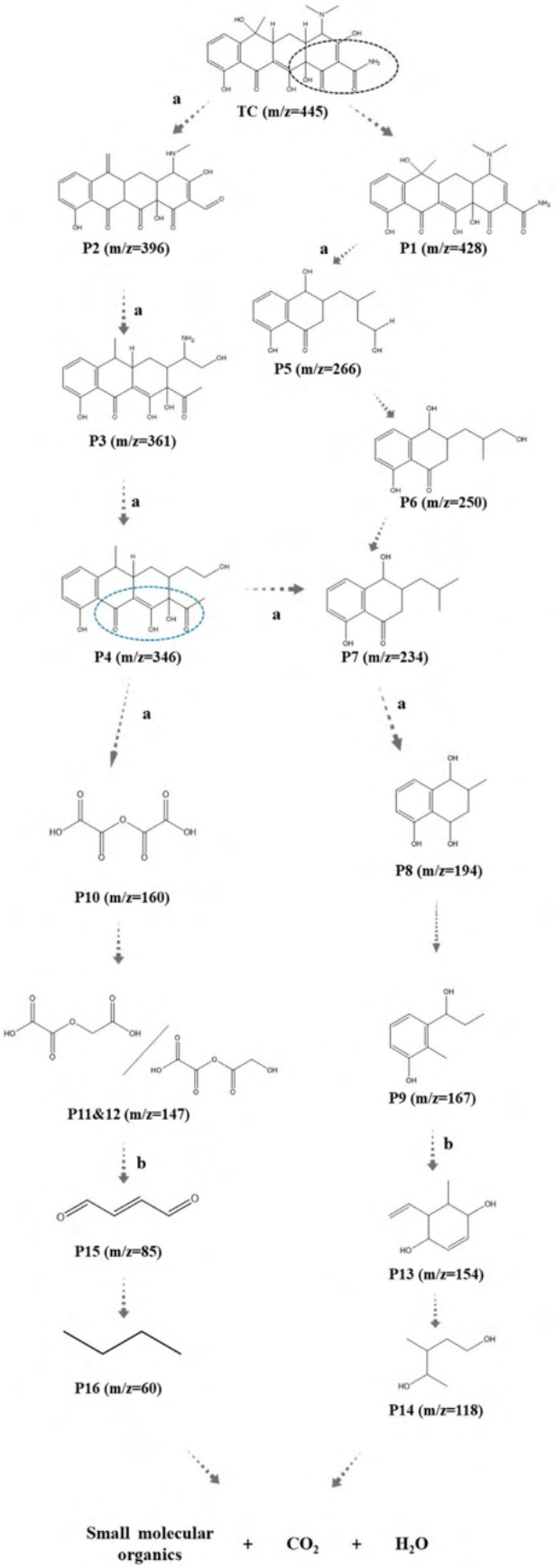

Fig. 10. Tetracycline degradation pathway on $ABC_{(25)}$ exposure (a: nucleophilic attack; b: free radical and electrophilic attack).

intermediates from P1 ($m/z = 428$) to P8 ($m/z = 194$) underwent a series of reactions, including ring-opening, which resulted in the degradation of the amino group. P2 ($m/z = 396$) transformed into P4 ($m/z = 346$) as the intermediate's ring structure broke, and the amino group was released from TC. In the progression from P4 ($m/z = 346$) to P8 ($m/z = 194$), the degradation primarily involved electrophilic reactions and free radical attacks. Some of P4 ($m/z = 346$) further degraded to P10 ($m/z = 160$), releasing one O atom and breaking the carbon-oxygen double bond, ultimately forming P11 and P12 ($m/z = 147$). Subsequently, a dehydration-condensation reaction occurred, producing P15 ($m/z = 85$) and, eventually, P16 ($m/z = 60$). Concurrently, an alternative pathway from P8 ($m/z = 194$) included a series of ring-opening reactions, resulting in intermediates P8 ($m/z = 194$), P9 ($m/z = 167$), P13 ($m/z = 154$), and P14 ($m/z = 118$). This pathway caused a reduction in the carbon chain length, ultimately generating smaller organic molecules, CO_2, and H_2O. To validate the degradation pathway, TOC analysis was conducted (Fig. 1c). Notably, the TOC degradation rate of TC by $ABC_{(25)}$ was high after 60 min of irradiation, indicating that most of the TC was effectively broken down into smaller organic molecules, CO_2, and H_2O [63]. This observation indicated the effectiveness of the degradation process in breaking down complex contaminants into simpler, less harmful substances.

The TC and its intermediates may present potential ecological risks, therefore, it is essential to predict their ecotoxicity. In this study, four representative toxicity factors were investigated, including *Daphnia magna* LD_{50} and Fathead minnow LD_{50}, which indicate acute toxicity, along with mutagenicity and developmental toxicity as chronic toxicity. As shown in Fig. 11a, the initial acute toxicity of TC to Fathead minnow was categorized as toxic, with an LD_{50} of 0.90 mg/L. After the initial stages of degradation, while the intermediate product P2 still exhibited some toxicity (LD_{50} of 0.47 mg/L), most subsequent intermediates showed a significant reduction in toxicity. For instance, the LD_{50} of P14 increased to 2014.77 mg/L, categorizing it was not harmful. Similarly, the acute toxicity for *Daphnia magna* showed a significant decrease after treatment with the optimized $ABC_{(25)}$ photocatalyst (Fig. 11b). Most intermediates exhibited progressively higher LD_{50} values, indicating a consistent reduction in toxicity. Notably, P9 exhibited an LD_{50} of 684.35 mg/L, indicating its negligible toxicity. This overall trend suggested that most TC degradation intermediates became less harmful with the photocatalytic degradation process.

In terms of chronic toxicity, mutagenicity and developmental toxicity were also analyzed (Fig. 11c and d). Except for slightly elevated toxicity for P2 in the early degradation stages, all the other intermediates exhibited mutagenicity/developmental toxicity negative results, indicating there was no significant mutagenic or developmental toxicity. Additionally, the TOC results (Fig. 1c) further confirmed the mineralization of TC into less harmful products by $ABC_{(25)}$, with a portion of the degradation byproducts being completely converted to CO_2 and water. This substantial reduction in both intermediate toxicity and TOC levels highlights the overall detoxification was achieved through the $ABC_{(25)}$ photocatalytic process. These findings demonstrated that the majority of intermediates formed during the degradation of TC were either non-toxic or exhibited reduced toxicity. This supported the conclusion that the $ABC_{(25)}$ photocatalyst efficiently degrades TC while ensuring a high level of ecological safety. Overall, the optimized $ABC_{(25)}$ photocatalyst provides an environmentally friendly and sustainable method for treating TC-containing wastewater, offering great potential for practical applications.

4. Conclusion

This study presents the successful synthesis of a novel ABC photocatalyst with remarkable TC degradation efficiency under solar irradiation. The optimized $ABC_{(25)}$ composite, harnessing an idea Z-scheme heterojunction, exhibited superior crystallinity, favorable structure and photocatalytic properties. These advantageous characteristics contribute to a 96.8 % TC degradation efficiency and high mineralization rate across

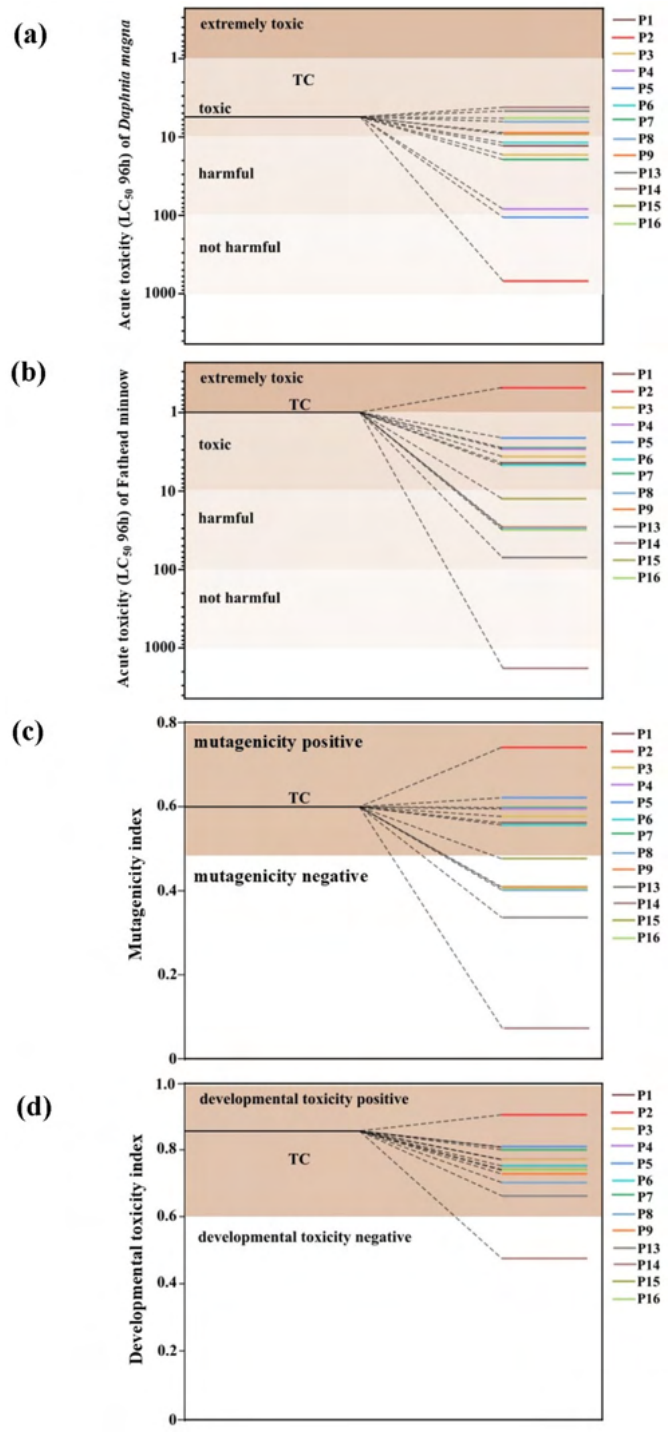

Fig. 11. Acute toxicity of (a) *Daphnia magna* LC_{50}, and (b) Fathead minnow LC_{50}, chronic toxicity of (c) mutagenicity and (d) developmental toxicity of tetracycline and degradation intermediates.

various environmental conditions. DFT calculations and toxicity assessments outlined the TC degradation pathway with reduced toxicity of TC intermediates, underscoring an environmentally safer process for antibiotic treatment. Therefore, the merits of high efficiency, robust environmental adaptability and stability make $ABC_{(25)}$ composite as an eco-friendly material for sustainable water treatment, addressing antibiotic contamination in real-world scenarios.

CRediT authorship contribution statement

Hongjian Zhang: Writing – original draft, Methodology, Investigation, Formal analysis, Data curation. **Qiansu Ma:** Writing – review & editing, Validation, Investigation, Formal analysis. **Guangqi An:** Writing – review & editing, Investigation, Formal analysis. **Yunxin Zhu:** Writing – review & editing, Validation. **Xiang Sun:** Formal analysis. **Naoki Kawazoe:** Writing – review & editing, Resources. **Guoping Chen:** Writing – review & editing, Supervision, Resources. **Yingnan Yang:** Writing – review & editing, Supervision, Resources, Project administration, Methodology, Funding acquisition, Data curation, Conceptualization.

Declaration of competing interest

The authors declare that they have no known competing financial interests or personal relationships that could have appeared to influence the work reported in this paper.

Acknowledgements

This research was supported by Scientific Research (B) 22H03778 and Grant-in-Aid for Exploratory Research 21k19628 from Japan Society for the Promotion of Science. The authors would like to thank National Institute of Materials Science (NIMS) for their technical support with characterization of photocatalyst materials.

Appendix A. Supplementary data

Supplementary data to this article can be found online at https://doi.org/10.1016/j.efmat.2024.12.004.

References

[1] A. Mann, K. Nehra, J.S. Rana, T. Dahiya, Antibiotic resistance in agriculture: perspectives on upcoming strategies to overcome upsurge in resistance, Curr. Res. Microb. Sci 2 (2021) 100030.
[2] Y.E. Messele, G.M. Werid, K. Petrovski, Meta-analysis on the global prevalence of tetracycline resistance in Escherichia coli isolated from beef cattle, Vet. Sci. 10 (2023) 479.
[3] G. Ferri, C. Lauteri, A. Vergara, Antibiotic resistance in the finfish aquaculture industry: a review, Antibiotics 11 (2022) 1574.
[4] Y. Pei, A. Lei, S. Yang, H. Chen, X. Liu, L. Liu, X. Kang, Biodegradation and bioaugmentation of tetracycline by Providencia stuartii TX2: performance, degradation pathway, genetic background, key enzymes, and application risk assessment, J. Hazard Mater. 477 (2024) 135231.
[5] J.E. Cevallos-Mendoza, G. Alay-Macias, F. Figueira, A.N. Araujo, C.G. Amorim, J.M. Rodríguez-Díaz, M.C.B.S.M. Montenegro, Nanocomposite HKUST-1@ polysulfone membrane for the adsorptive removal of tetracyclines in waters, Sep. Purif. Technol. 330 (2024) 125568.
[6] L. Wang, Y. Zhao, M. Sun, Y. Zheng, H. Fan, S. Wang, C. Jiang, Bifunctional sulfur-doped biochar for efficient removal of tetracycline and resistant bacteria via adsorption and peroxydisulfate activation, Sep. Purif. Technol. 354 (2025) 128728.
[7] S. Li, C. You, Q. Xue, Y. Zhao, F. Yang, Y. Liu, L. Bai, M. Zhang, C. Zhuang, Carbon quantum dots and interfacial chemical bond synergistically modulated S-scheme $Mn_{0.5}Cd_{0.5}S$/BiOBr photocatalyst for efficient water purification, J. Mater. Sci. Technol. 214 (2025) 255–265.
[8] S. Li, C. Wang, K. Dong, P. Zhang, X. Chen, X. Li, MIL-101(Fe)/BiOBr S-scheme photocatalyst for promoting photocatalytic abatement of Cr(VI) and enrofloxacin antibiotic: performance and mechanism, Chin. J. Catal. 51 (2023) 101–112.
[9] C. Sivaraman, S. Vijayalakshmi, E. Leonard, S. Sagadevan, R. Jambulingam, Current developments in the effective removal of environmental pollutants through photocatalytic degradation using nanomaterials, Catalysts 12 (2022) 544.
[10] A. Balapure, J. Ray Dutta, R. Ganesan, Recent advances in semiconductor heterojunctions: a detailed review of the fundamentals of photocatalysis, charge transfer mechanism and materials, RSC Applied Interfaces 1 (2024) 43–69.
[11] S.K. Srivastava, Recent advances in removal of pharmaceutical pollutants in wastewater using metal oxides and carbonaceous materials as photocatalysts: a review, RSC Applied Interfaces 1 (2024) 340–429.
[12] X. Hu, Q. Ma, X. Wang, Y. Yang, N. Liu, C. Zhang, N. Kawazoe, G. Chen, Y. Yang, Layered $Ag/Ag_2O/BiPO_4/Bi_2WO_6$ heterostructures by two-step method for enhanced photocatalysis, J. Catal. 387 (2020) 28–38.
[13] X. Hu, Q. Zhu, X. Wang, N. Kawazoe, Y. Yang, Nonmetal–metal–semiconductor-promoted $P/Ag/Ag_2O/Ag_3PO_4/TiO_2$ photocatalyst with superior photocatalytic activity and stability, J. Mater. Chem. A Mater. 3 (2015) 17858–17865.

[14] Q. Zhu, N. Liu, Q. Ma, A. Sharma, D. Nagai, X. Sun, C. Zhang, Y. Yang, Sol-gel/hydrothermal two-step synthesis strategy for promoting Ag species–modified TiO_2-based composite activity toward H_2 evolution under solar light, Mater. Today Energy 20 (2021) 100648.

[15] Y. Lan, Z. Li, D. Li, W. Xie, G. Yan, S. Guo, Visible-light responsive Z-scheme Bi@β-Bi_2O_3/g-C_3N_4 heterojunction for efficient photocatalytic degradation of 2,3-dihydroxynaphthalene, Chem. Eng. J. 392 (2020) 123686.

[16] M. Cai, Y. Liu, K. Dong, X. Chen, S. Li, Floatable S-scheme Bi_2WO_6/C_3N_4/carbon fiber cloth composite photocatalyst for efficient water decontamination, Chin. J. Catal. 52 (2023) 239–251.

[17] S. Li, K. Dong, M. Cai, X. Li, X. Chen, A plasmonic S-scheme Au/MIL-101(Fe)/BiOBr photocatalyst for efficient synchronous decontamination of Cr(VI) and norfloxacin antibiotic, eScience 4 (2024) 100208.

[18] J. Zhang, J. Wei, M. Xiahou, Z. Sun, A. Cao, Y. Yuanfeng, Y. He, S. Song, Direct Z-scheme In_2S_3@$BiYWO_6$ heterojunction photocatalysts for highly efficient environmental remediation, Appl. Surf. Sci. 651 (2024) 159197.

[19] K. Saravanakumar, C.M. Park, Rational design of a novel $LaFeO_3$/g-C_3N_4/$BiFeO_3$ double Z-scheme structure: photocatalytic performance for antibiotic degradation and mechanistic insight, Chem. Eng. J. 423 (2021) 130076.

[20] B. Chong, L. Chen, W. Wang, D. Han, L. Wang, L. Feng, Q. Li, C. Li, Visible-light-driven Ag-decorated g-C_3N_4/Bi_2WO_6 Z-scheme composite for high photocatalytic activity, Mater. Lett. 204 (2017) 149–153.

[21] C. Zhang, Y. Li, D. Shuai, Y. Shen, W. Xiong, L. Wang, Graphitic carbon nitride (g-C_3N_4)-based photocatalysts for water disinfection and microbial control: a review, Chemosphere 214 (2019) 462–479.

[22] Z. Jiang, J. Xie, *In situ* growth of Ag/Ag_2O nanoparticles on g-C_3N_4 by a natural carbon nanodot-assisted green method for synergistic photocatalytic activity, RSC Adv. 6 (2016) 3186–3197.

[23] C. Wu, H. Zuo, H. Du, S. Zhang, L. Wang, Q. Yan, Construction of layered embedding dual Z-scheme $Bi_2O_2CO_3$/g-C_3N_4/Bi_2O_3: tetracycline degradation pathway, toxicity analysis and mechanism insight, Sep. Purif. Technol. 282 (2022) 120096.

[24] J. Chen, Q. Yang, J. Zhong, J. Li, C. Hu, Z. Deng, R. Duan, *In-situ* construction of direct Z-scheme Bi_2WO_6/g-C_3N_4 composites with remarkably promoted solar-driven photocatalytic activity, Mater. Chem. Phys. 217 (2018) 207–215.

[25] T. Lu, F. Chen, Multiwfn: a multifunctional wavefunction analyzer, J. Comput. Chem. 33 (2012) 580–592.

[26] Q. Ni, X. Ke, W. Qian, Z. Yan, J. Luan, W. Liu, Insight into tetracycline photocatalytic degradation mechanism in a wide pH range on BiOI/BiOBr: coupling DFT/QSAR simulations with experiments, Appl. Catal., B 340 (2024) 123226.

[27] C. Liu, J. Jin, F. Dong, Z. Zhang, D. Zhou, M. Jin, H. Wan, M. Shao, Y. Wan, Synthesis of a novel NiCo-LDH/Bi_2WO_6 Z-scheme heterojunction composite for photocatalytic degradation of tetracycline, J. Alloys Compd. 1008 (2024) 176838.

[28] P. Xiao, C. Shen, Y. Li, S. Cui, S. Chen, J. Yang, A one-pot hydrothermal synthesis of Bi/$Bi_2O_2CO_3$/Bi_2WO_6 catalyst with enhanced photocatalytic activity to tetracycline, J. Taiwan Inst. Chem. Eng. 162 (2024) 105611.

[29] H. Zhao, T. He, Q. Zhang, H. Feng, H. Mi, Z. Liang, D. Zhou, W. Dong, X. Xue, Interfacial bonded K-doped-C_3N_4@Bi_2WO_6 heterostructure for efficient photocatalytic degradation of tetracycline, J. Alloys Compd. 972 (2024) 172822.

[30] J. Jin, M. Xu, F. Dong, H. Hu, Y. Yang, W. Jin, Z. Zhang, M. Shao, Y. Wan, Synthesis of novel Cu_2WS_4/Bi_2WO_6 heterojunctions and evaluation of their photocatalytic activity for removal of tetracycline under visible light irradiation, Opt. Mater. 147 (2024) 114700.

[31] K. Althumayri, A. Guesmi, W.A. El-Fattah, A. Houas, N. Ben Hamadi, A. Shahat, Enhanced adsorption and evaluation of tetracycline removal in an aquatic system by modified silica nanotubes, ACS Omega 8 (2023) 6762–6777.

[32] Z. Li, L. Schulz, C. Ackley, N. Fenske, Adsorption of tetracycline on kaolinite with pH-dependent surface charges, J. Colloid Interface Sci. 351 (2010) 254–260.

[33] Changing ocean, marine ecosystems, and dependent communities, in: The Ocean and Cryosphere in a Changing Climate, Cambridge University Press, 2022, pp. 447–588.

[34] H. Ishida, R.S. Isono, J. Kita, Y.W. Watanabe, Long-term ocean acidification trends in coastal waters around Japan, Sci. Rep. 11 (2021) 5052.

[35] Ocean, cryosphere and sea level change, in: Climate Change 2021 – the Physical Science Basis, Cambridge University Press, 2023, pp. 1211–1362.

[36] C. Zhang, G. An, Y. Zhu, X. Sun, G. Chen, Y. Yang, Development of a sunlight adjustable parabolic trough reactor for 24-hour efficient photocatalytic wastewater treatment, Chem. Eng. J. 497 (2024) 154582.

[37] Y. Zhang, C. Lin, Q. Lin, Y. Jin, Y. Wang, Z. Zhang, H. Lin, J. Long, X. Wang, CuI-BiOI/Cu film for enhanced photo-induced charge separation and visible-light antibacterial activity, Appl. Catal., B 235 (2018) 238–245.

[38] M. Huang, J. Li, Y. Huang, X. Zhou, Z. Qin, Z. Tong, M. Fan, B. Li, L. Dong, Construction of g-C_3N_4 based heterojunction photocatalyst by coupling TiO_2-SnO_2 solid solution for efficient multipurpose photocatalysis, J. Alloys Compd. 864 (2021) 158132.

[39] C. You, C. Wang, M. Cai, Y. Liu, B. Zhu, S. Li, Improved photo-carrier transfer by an internal electric field in BiOBr/N-rich C_3N_5 3D/2D S-scheme heterojunction for efficiently photocatalytic micropollutant removal, Acta Physico, Chimica. Sinica. 0 (2024) 2407014.

[40] S. Li, C. You, K. Rong, C. Zhuang, X. Chen, B. Zhang, Chemically bonded $Mn_{0.5}Cd_{0.5}S$/BiOBr S-scheme photocatalyst with rich oxygen vacancies for improved photocatalytic decontamination performance, Adv. Powder Mater. 3 (2024) 100183.

[41] J. Ruan, T. Zhong, Y. Guo, Enhanced water splitting over ethylenediaminetetraacetate treated $SrTiO_3$ photocatalysts with high crystallinity, reduced size, and surface nanostructure, J. Colloid Interface Sci. 650 (2023) 1424–1433.

[42] Z. Wang, T. Hu, K. Dai, J. Zhang, C. Liang, Construction of Z-scheme Ag_3PO_4/Bi_2WO_6 composite with excellent visible-light photodegradation activity for removal of organic contaminants, Chin. J. Catal. 38 (2017) 2021–2029.

[43] X. Zeng, S. Shu, Y. Meng, H. Wang, Y. Wang, Enhanced photocatalytic degradation of sulfamethazine by g-C_3N_4/Cu, N-TiO_2 composites under simulated sunlight irradiation, Chem. Eng. J. 456 (2023) 141105.

[44] C. Li, G. Chen, J. Sun, J. Rao, Z. Han, Y. Hu, W. Xing, C. Zhang, Doping effect of phosphate in Bi_2WO_6 and universal improved photocatalytic activity for removing various pollutants in water, Appl. Catal., B 188 (2016) 39–47.

[45] Y. Che, B. Lu, Q. Qi, H. Chang, J. Zhai, K. Wang, Z. Liu, Bio-inspired Z-scheme g-C_3N_4/Ag_2CrO_4 for efficient visible-light photocatalytic hydrogen generation, Sci. Rep. 8 (2018) 16504.

[46] N. Liu, N. Lu, H. Yu, S. Chen, X. Quan, Enhanced degradation of organic water pollutants by photocatalytic *in-situ* activation of sulfate based on Z-scheme g-C_3N_4/$BiPO_4$, Chem. Eng. J. 428 (2022) 132116.

[47] A. Elaouni, M. El Ouardi, A. BaQais, M. Arab, M. Saadi, H. Ait Ahsaine, Bismuth tungstate Bi_2WO_6: a review on structural, photophysical and photocatalytic properties, RSC Adv. 13 (2023) 17476–17494.

[48] L. Zhang, K.H. Wong, Z. Chen, J.C. Yu, J. Zhao, C. Hu, C.Y. Chan, P.K. Wong, AgBr-Ag-Bi_2WO_6 nanojunction system: a novel and efficient photocatalyst with double visible-light active components, Appl. Catal. Gen. 363 (2009) 221–229.

[49] J. Ren, W. Wang, S. Sun, L. Zhang, J. Chang, Enhanced photocatalytic activity of Bi_2WO_6 loaded with Ag nanoparticles under visible light irradiation, Appl. Catal., B 92 (2009) 50–55.

[50] X. Yuan, S. Qu, X. Huang, X. Xue, C. Yuan, S. Wang, L. Wei, P. Cai, Design of core-shelled g-C_3N_4@ZIF-8 photocatalyst with enhanced tetracycline adsorption for boosting photocatalytic degradation, Chem. Eng. J. 416 (2021) 129148.

[51] J. Yu, S. Wang, J. Low, W. Xiao, Enhanced photocatalytic performance of direct Z-scheme g-C_3N_4–TiO_2 photocatalysts for the decomposition of formaldehyde in air, Phys. Chem. Chem. Phys. 15 (2013) 16883.

[52] L. Ge, C. Han, J. Liu, Novel visible light-induced g-C_3N_4/Bi_2WO_6 composite photocatalysts for efficient degradation of methyl orange, Appl. Catal., B 108–109 (2011) 100–107.

[53] Q. Ma, J. Ming, X. Sun, N. Liu, G. Chen, Y. Yang, Visible light active graphene oxide modified Ag/Ag_2O/$BiPO_4$/Bi_2WO_6 for photocatalytic removal of organic pollutants and bacteria in wastewater, Chemosphere 306 (2022) 135512.

[54] H. Mou, C. Song, Y. Zhou, B. Zhang, D. Wang, Design and synthesis of porous Ag/ZnO nanosheets assemblies as super photocatalysts for enhanced visible-light degradation of 4-nitrophenol and hydrogen evolution, Appl. Catal., B 221 (2018) 565–573.

[55] F. Yang, J. Qu, Y. Zheng, Y. Cai, X. Yang, C.M. Li, J. Hu, Recent advances in high-crystalline conjugated organic polymeric materials for photocatalytic CO_2 conversion, Nanoscale 14 (2022) 15217–15241.

[56] H. Yu, R. Liu, X. Wang, P. Wang, J. Yu, Enhanced visible-light photocatalytic activity of Bi_2WO_6 nanoparticles by Ag_2O cocatalyst, Appl. Catal., B 111–112 (2012) 326–333.

[57] J. Ming, X. Sun, Q. Ma, N. Liu, C. Zhang, N. Kawazoe, G. Chen, Y. Yang, Advanced photocatalytic sterilization for recalcitrant Enterococcus sp. contaminated water by newly developed Z-scheme Bi_2WO_6 based composites under solar light, Chemosphere 310 (2023) 136912.

[58] P. Xia, B. Zhu, B. Cheng, J. Yu, J. Xu, 2D/2D g-C_3N_4/MnO_2 Nanocomposite as a direct Z-scheme photocatalyst for enhanced photocatalytic activity, ACS Sustain. Chem. Eng. 6 (2018) 965–973.

[59] D. Kanakaraju, J. Kockler, C.A. Motti, B.D. Glass, M. Oelgemöller, Titanium dioxide/zeolite integrated photocatalytic adsorbents for the degradation of amoxicillin, Appl. Catal., B 166–167 (2015) 45–55.

[60] C. Loka, K.-S. Lee, Enhanced visible-light-driven photocatalysis of Ag/Ag_2O/ZnO nanocomposite heterostructures, Nanomaterials 12 (2022) 2528.

[61] A. Ahmadi, M. Hajilou, S. Zavari, S. Yaghmaei, A comparative review on adsorption and photocatalytic degradation of classified dyes with metal/non-metal-based modification of graphitic carbon nitride nanocomposites: synthesis, mechanism, and affecting parameters, J. Clean. Prod. 382 (2023) 134967.

[62] X. Xiao, H. Wang, X. Wang, C. Liu, Y. Han, S. Zhai, H. Du, Innovative lignin photocatalyst system motivated by intramolecular charge dynamics for H_2O_2 production, Chem. Eng. J. 494 (2024) 153151.

[63] X. Li, Y. Huang, W. Ho, S. Han, P. Wang, S. Lee, Z. Zhang, Modulation of sulfur vacancies at $ZnIn_2S_4$-δ/g-C_3N_4 heterojunction interface for successive C-H secession in photocatalytic gaseous formaldehyde complete oxidation, Appl. Catal., B 338 (2023) 123048.